Current Science
CS 5 (3), 2479-2491 (2025)
Received 24 Feb 2025 | **Revised 21 March** 2025 | **Accepted 22 April**. 2025 | **Online Available 20 May** 2025
https://doi.org/ 10.52845/CS/2025-5-3-34

Current Science

Current Science

OPEN ACCESS

ISSN (O) 2795-8639

Original Article

Structure, Magnetic Properties and Electromagnetic Wave Absorption Properties of $Bi_{1-X}y_xfeo_3$

Yuanhang Gao*[1], Zesheng Li[1], Jinxiang Guo[1], Fangyu Gan*[1], Qingrong Yao*[1], Lichun Cheng[1], Jianqiu Deng[1], Yan Zhong[1], Zhao Lu[1], Huaiying Zhou[1]

[1]**School of Materials Science and Engineering, Guilin University of Electronic Technology, Guilin, 541004, PR, China**

[*]**Corresponding Author: Yuanhang Gao, Fangyu Gan, Qingrong Yao**

Abstract:
Rare earth ion doping in ferrites has been recognized as an effective method for modulating the dielectric and magnetic properties of ferrites. In this work, Y-doped $BiFeO_3$ samples were successfully synthesized via the sol-gel method. The influence of Y doping concentration (x = 0, 0.05, 0.10, and 0.15) on the crystal structure, microstructure, magnetic properties, and electromagnetic wave absorption (EMW) performance of $BiFeO_3$ was systematically examined. XRD results indicate a phase transition in $BiFeO_3$ from R3c (rhombohedral) to Pbnm (orthorhombic) with increasing Y doping concentration, accompanied by reductions in lattice parameters, unit cell volume, and grain size. The saturation magnetization increases first and then decreases with the increase of Y^{3+} doping content, and reaches the maximum value when x = 0.10. Rietveld refinement reveals that Y^{3+} doping induces tilting of FeO_6 octahedra, which is attributed to the enhancement of saturation magnetization. A synergistic effect of dielectric and magnetic losses leads to a minimum reflection loss of –35.19 dB at 2.2 mm and a maximum effective absorption bandwidth of 3.29 GHz for $Bi_{0.90}Y_{0.10}FeO_3$.

Keywords: $BiFeO_3$; Rare-earth yttrium doping; Magnetic properties; Electromagnetic wave absorption performance

Introduction

Accompanying the explosive development of electronic device and wireless communication technology working at GHz range, highly efficient electromagnetic wave absorption (EMA) materials have drawn increasing attention [1-3]. EMA materials are constantly being developed to meet the requirements of thin thickness, light weight, and broad bandwidth [4-6]. Ferrites have been considered as the most potential candidate for EMA materials due to their advantages of potential permeability, permittivity, and rich resources. In recent year, tremendous effort has been thrown into the research of ferrites in the field of EMA absorption. Wang et al. prepared Sr doped $YFeO_3$ and obtained excellent EMA performance with a reflection loss (RL) value of –30.87 dB [7]. Huang et al. synthesized Sr doped $LaFeO_3$ with a minimum RL of –30.04 dB and an effective absorption bandwidth (EAB) of 2.1 GHz [8]. Hu et al. prepared $BaFe_{12}O_{19}/MnO_2$ composites with the RL of –54.39 dB [9]. Among the ferrites, $BiFeO_3$, a unique room temperature single-phase multiferroic, has attracted great attention due to its long range magnetic and electric ordering. Moreover, the unique magnetoelectric coupling and crystal structure can generate ferroelectricity and ferromagnetism which is beneficial to attenuate the incident electromagnetic wave (EMW) [10]. The lone pair electron in the outer shell of Bi^{3+} ions induce ferroelectricity, while the exchange interaction of Fe−O−Fe produces antiferromagnetic properties [11, 12]. It is well known that magnetic loss and dielectric loss are determined loss mechanism for attenuated EMW energy [13-15]. However, the spatially modulated spiral spin structure with a

period of 62 nm of $BiFeO_3$ inhibit the net magnetic moment, inducing the weak magnetism on the macro level [16, 17]. Hence, pure $BiFeO_3$ exhibit poor EMA performance. To improve the EMA performance of $BiFeO_3$, various strategies such as element doping, composition regulation and structure design were adopted [18].

Rare earth (RE) elements have many excellent optical, magnetic, and electric properties due to the special atomic structure and the diversity of electronic energy levels [19-21]. The RE ion substitution can fundamentally change the crystal structure of $BiFeO_3$, and further affect the magnetic and dielectric properties. Owing to the structure distortion induced by unequal ion radii, the RE ions substitution may contribute to adjust magnetic interactions, and therefore improve the magnetic properties. In addition, the unpaired 4f electrons of RE ions cause angular momentum coupling, which affects the dielectric properties of the doped matrix. As previously reported, RE ion doping effectively regulated the magnetic and dielectric properties of $BiFeO_3$, thus improve the EMA performance. Guo et al. enhanced magnetic properties of $BiFeO_3$ through doping Pr in the Bi site and a wide EAB of 3.41 GHz can be obtained [22]. Yan et al. prepared Dy doped $BiFeO_3$ samples by a solid-state reaction method. The magnetic moment and radius of Dy^{3+} ions played vital role in the crystal structural evolution and multiferroic properties of $BiFeO_3$ [23]. Li et al. studied the ferromagnetic properties and EMA properties of La doped $BiFeO_3$ samples [24].

Till now, most of the research has focused on the ferromagnetic properties of $BiFeO_3$, while little have been done to elucidate the EMA performance and the loss mechanism. Reports devoted on RE ions doped $BiFeO_3$ and applied in the field of EMA have been very limited. The relationship between the crystal structure, morphology, magnetic properties, and EMA properties of Y doped $BiFeO_3$ is still unclear. Therefore, it is necessary to study the influence of the substitution of Y on the crystal structure, magnetic properties, and EMA properties of $BiFeO_3$. In this work, series of Y doped $BiFeO_3$ samples were synthesized by sol-gel method and subsequent sintering process. The microstructure, crystal structure, magnetic properties, EMA performance, and EMW loss mechanism of $Bi_{1-x}Y_xFeO_3$ were systematically studied.

2. Materials and Methods

2.1. Preparation of $Bi_{1-x}Y_xFeO_3$ (x = 0, 0.05, 0.10, 0.15) Samples

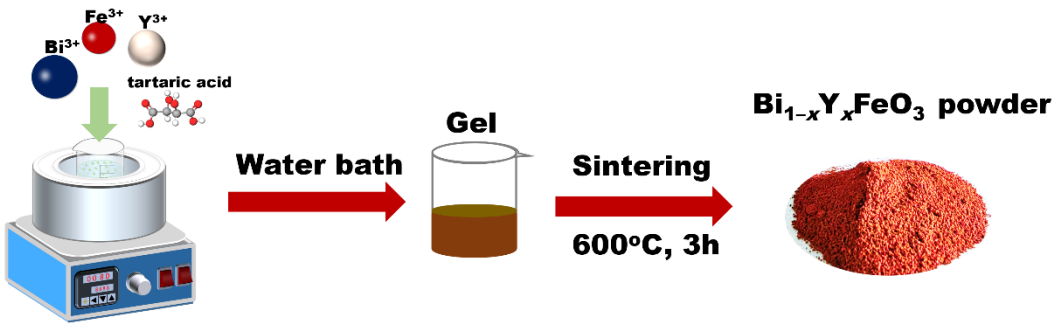

Figure 1. Schematic illustration of the preparation process of $Bi_{1-x}Y_xFeO_3$.

$Bi_{1-x}Y_xFeO_3$ (x = 0, 0.05, 0.10, 0.15) were prepared by sol-gel method and subsequent calcination process. The preparation process is showed in **Fig.1**. High-purity $Fe(NO_3)_3{\cdot}9H_2O$ (Aladdin, 98.5%), $Y(NO_3)_3{\cdot}6H_2O$ (Aladdin, 99%), $Bi(NO_3)_3{\cdot}5H_2O$ (Xilong, scientific, 99%, excess 2%) and $C_4H_6O_6$ (Xilong scientific, 99%) were used without any purification. A typical preparation rout described as follow: the weights of $Y(NO_3)_3{\cdot}6H_2O$, $Fe(NO_3)_3{\cdot}9H_2O$ and $Bi(NO_3)_3{\cdot}5H_2O$ were calculated according to stoichiometric ratio of $Bi_{1-x}Y_xFeO_3$ (x = 0, 0.05, 0.10, 0.15). A dilute nitric acid solution was first prepared to prevent the precipitation of Bi $(OH)_3$. The ratio of deionized water to nitric acid was 4:1. $Y(NO_3)_3{\cdot}6H_2O$, $Fe(NO_3)_3{\cdot}9H_2O$ and $Bi(NO_3)_3{\cdot}5H_2O$ and $C_4H_6O_6$ were dissolved in 50 mL dilute nitric acid solution, and the molar ratio of metal cation to $C_4H_6O_6$ was 1:1. Then, the mixed solution was stirred at 80 °C for 3 h to get a wet gel precursor. The gel was dry in an air-

circulating oven at 100 ℃ overnight. Finally, the final products were obtained by sintering the precursor in muffle furnace at 600 ℃ for 3h with a heating rate of 2 ℃/min.

2.2. Characterization

The phase composition and structure of $Bi_{1-x}Y_xFeO_3$ was measured via high-resolution powder X-ray diffractometer (XRD, PANalytical PIXcel3D) with copper Kα radiation. The scan rate was 20 s per degree. The morphology was observed through the field emission scanning electron microscope (FE-SEM, FEI Quanta FEG 450). The element valence states of $Bi_{1-x}Y_xFeO_3$ were detected via X-ray photoelectron spectroscopy (XPS, Thermo Scientific K-Alpha$^+$ spectrometer). The hysteresis loop of the samples at room temperature were measured via the magnetometer (VSM, 7400-S, Lake Shore Cryotronics, USA). The electromagnetic parameters were collected via vector network analyzer (VNA, N5230C, Agilent, USA) using a coaxial method. The toroidal specimen was prepared by fully mixing the samples with paraffin. The outer diameter and inner diameter of toroidal specimen was 7.00 mm and 3.0 mm, respectively.

3. Results and Discussion

3.1. Phase and Structure

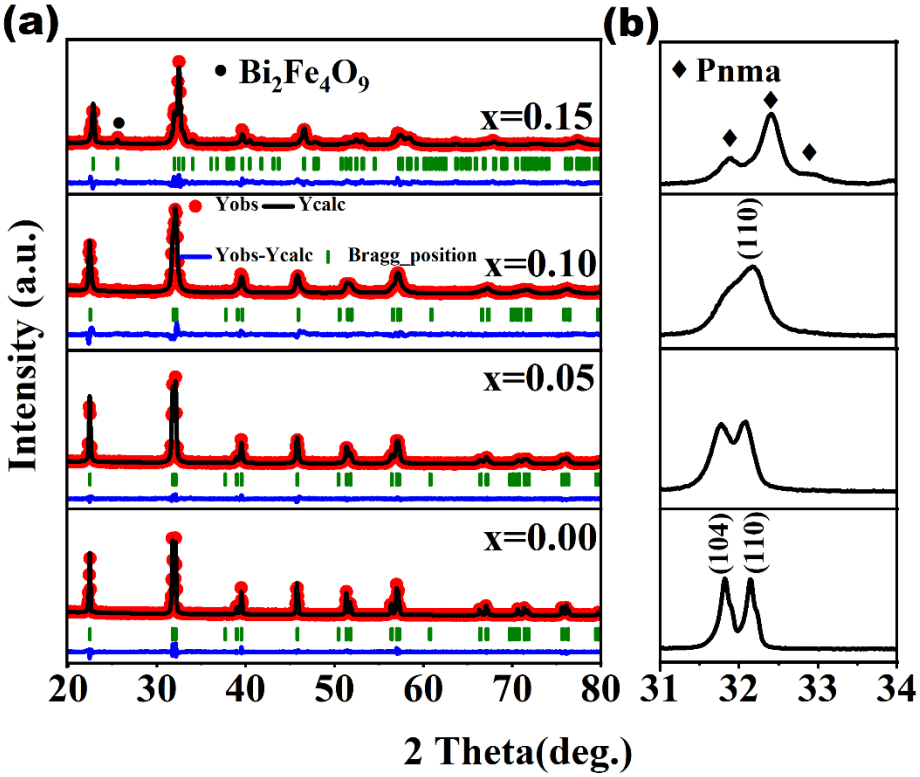

Figure 2. (a) XRD pattern of $Bi_{1-x}Y_xFeO_3$ and (b) magnified view of the peaks from 31° to 34°.

XRD spectrum was applied to detect the phase and crystal structure of $Bi_{1-x}Y_xFeO_3$ (x = 0, 0.05, 0.1, and 0.15). The Fullprof software was used for Rietveld fitting of the XRD spectrum, as shown in **Fig. 2**(a). Experimental pattern is black curve while the calculated pattern and their differences are given in red and green colors, respectively. The experimental pattern is agreement well with the calculation pattern. As the doping amount of Y is increased from 0 to 0.15, $Bi_{1-x}Y_xFeO_3$ undergone two structural transitions, from rhombohedral R3c phase at x = 0.00 and 0.05 to pseudo-cubic Pm-3m phase at x = 0.10, and finally to orthorhombic Pnma phase at x = 0.15 [23, 25]. Besides, a second phase, $Bi_2Fe_4O_9$, is found in $Bi_{0.85}Y_{0.15}FeO_3$, suggesting that high Y doping content may make the orthorhombic phase of $BiFeO_3$ unstable. The large structural transformation in the narrow range of Y doping may be related to the large difference in radius between Y^{3+} and Bi^{3+}. Similar phenomenon was found in Ho and Dy replacing the A-site of $BiFeO_3$ [23, 26]. The occurrence of the orthorhombic phase might change the ferromagnetic properties of the $Bi_{1-x}Y_xFeO_3$, due

to the higher symmetry of the orthorhombic phase. The Y^{3+} (1.02 Å) replaced of Bi^{3+} (1.17Å) lead to the change in lattice parameters, bond length and bond angle, thus resulting in the phase transformation. Cell parameters obtained by Rietveld fitting of the XRD patterns are depicted in **Table 1**. The lattice constant and unit cell volume decrease with the increase of Y doping content, which is consistent with the experiment XRD pattern.

Table 1 Unit cell parameters and crystal structure of the samples

Sample	Space group	Lattice parameters (Å)			Unit cell volume (Å3)	R_{exp}	χ^2
		a	b	c			
x=0.00	R3c	5.5794	5.5794	13.8727	374.011(8)	10.3	3.03
x=0.05	R3c	5.5767	5.5767	13.8612	373.323(9)	12.5	1.07
x=0.10	Pm-3m	5.5609	5.5609	13.8013	369.611(6)	18.3	1.92
x=0.15	Pnma	5.4537	5.6073	7.8053	238.681(1)	20.9	2.25

3.2. Element Valence State Analysis

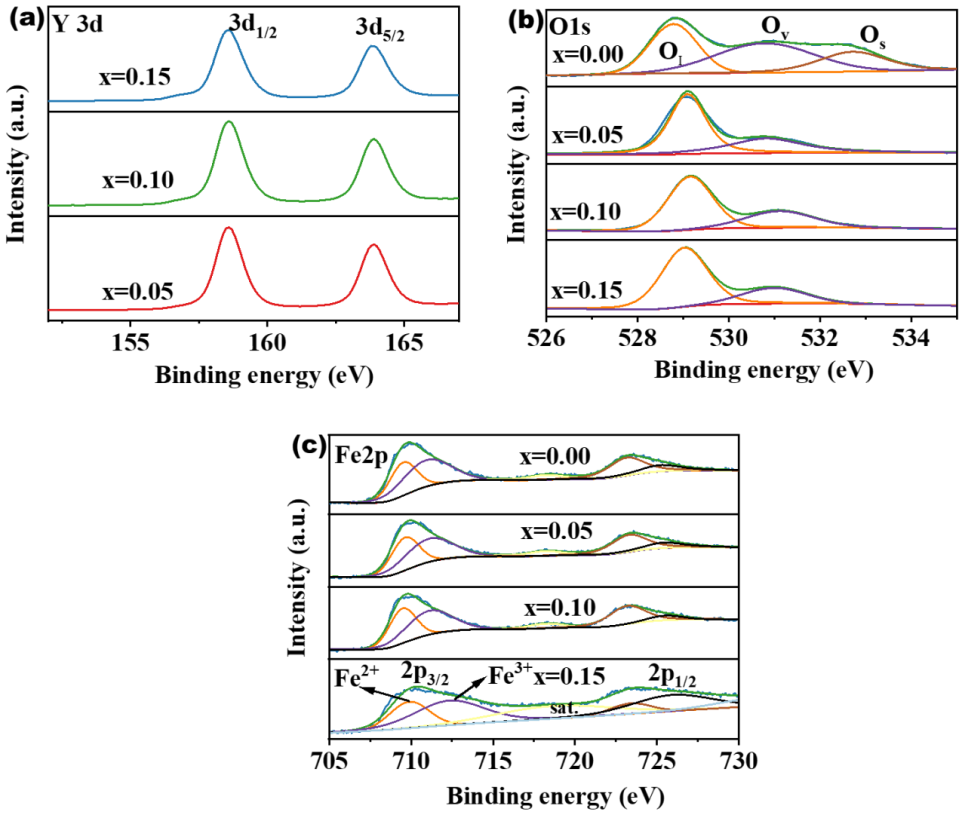

Figure 3. XPS spectra of (a) Y 3d, (b) O ls, and (c) Fe 2p.

XPS was applied to study the chemical valence states of the $Bi_{1-x}Y_xFeO_3$ (x = 0, 0.05, 0.1, and 0.15) powders. As shown in Fig. 3(a), the peaks of Y 3d at 158.38 and 163.39 eV is corresponded to Y 3d3/2 and Y 3d5/2, respectively, confirming the existence of Y^{3+} [7]. In the O ls spectrum of $Bi_{1-x}Y_xFeO_3$ sample (Fig. 3(b)), it can be clearly found that the O 1s peak of $Bi_{1-x}Y_xFeO_3$ sample is asymmetric, which is usually attributed to oxygen vacancy [27]. The high-resolution O 1s spectra of $Bi_{1-x}Y_xFeO_3$ nanoparticles can be divided into three peaks, representing lattice oxygen (O_I at 528.79 eV), oxygen vacancy (O_v at 530.72 eV) and chemisorbed oxygen (O_s at 532.7eV), respectively [28]. The calculation results of O_v peak area show that the proportion of oxygen vacancy gradually decrease from 44.3% to 24.6%

with the increase of Y doping amount. The reduction of oxygen vacancy may be due to the partial substitution of Y element at the A site of $BiFeO_3$, which inhibits the volatilization of Bi element [16, 29]. The variation of oxygen vacancy will further affect the valence state undulation of Fe ion in $BiFeO_3$. The XPS spectrum of Fe 2p is shown in Fig. 3(c). The peaks at 709.9 and 723.4 eV correspond to the characteristic peaks of Fe 2p3/2 and Fe 2p1/2, respectively [30, 31]. The fitting data of Fe 2p peaks indicate that Fe^{2+} and Fe^{3+} valence states coexist in $Bi_{1-x}Y_xFeO_3$ nanoparticles, and the Fe^{2+} content decreases with the increase of Y^{3+} ratio. The calculated peak area of Fe^{2+} in $BiFeO_3$, $Bi_{0.95}Y_{0.05}FO_3$, $Bi_{0.90}Y_{0.10}FO_3$ and $Bi_{0.85}Y_{0.15}FO_3$ account for 50.6%, 42.6%, 39.6% and 36.6% of the total Fe ions, respectively, which again confirms that Y doped in $BiFeO_3$ can effectively reduce oxygen vacancy.

3.3. Micro-Morphology Analysis

The micro-morphology of $Bi_{1-x}Y_xFeO_3$ powders were investigated by SEM. As shown in **Fig. 4**(a), the undoped $BiFeO_3$ exhibit cubic-like nano-particles with an average size of 0.40 μm. The substitution of Y^{3+} has a significant effect on the morphology of $BiFeO_3$, which changes from cube to irregular ellipsoid. From Fig. 4(b–d), the grain size decrease with the increase of the Y doping content. The grain sizes of $Bi_{0.95}Y_{0.05}FeO_3$, $Bi_{0.90}Y_{0.10}FeO_3$ and $Bi_{0.85}Y_{0.15}FeO_3$ are 0.19 μm, 0.16 μm and 0.15 μm, respectively. For $BiFeO_3$, the low melting point of Bi_2O_3 leads to volatilization of Bi elements and plentiful oxygen vacancy are generated in sintering process at high temperature. Oxygen vacancy improves ion migration rate and promotes grain growth [7]. The XPS results show that Y substituted Bi suppress the oxygen vacancy, which prevent the ions movement, and then inhibit the grain growth. Moreover, the pinning effect of RE on grains also affected the growth of grain [22]. Notably, the smaller the grain size, the more easily the defects accumulate at the grain boundary, which has an important effect on the magnetic crystal anisotropy, and thus affect the magnetic properties [32]. In addition, the smaller the grain size is, the more heterogeneous interface are formed, which is very favorable to the attenuation of EMW energy. The crystal structure of $Bi_{0.90}Y_{0.10}FeO_3$ was further study via TEM, as shown in Fig. 4(e–g). The lattice fringe in the grain is about 0.276 nm, assigning to the (110) plane of $BiFeO_3$, which is in consistent with the XRD result.

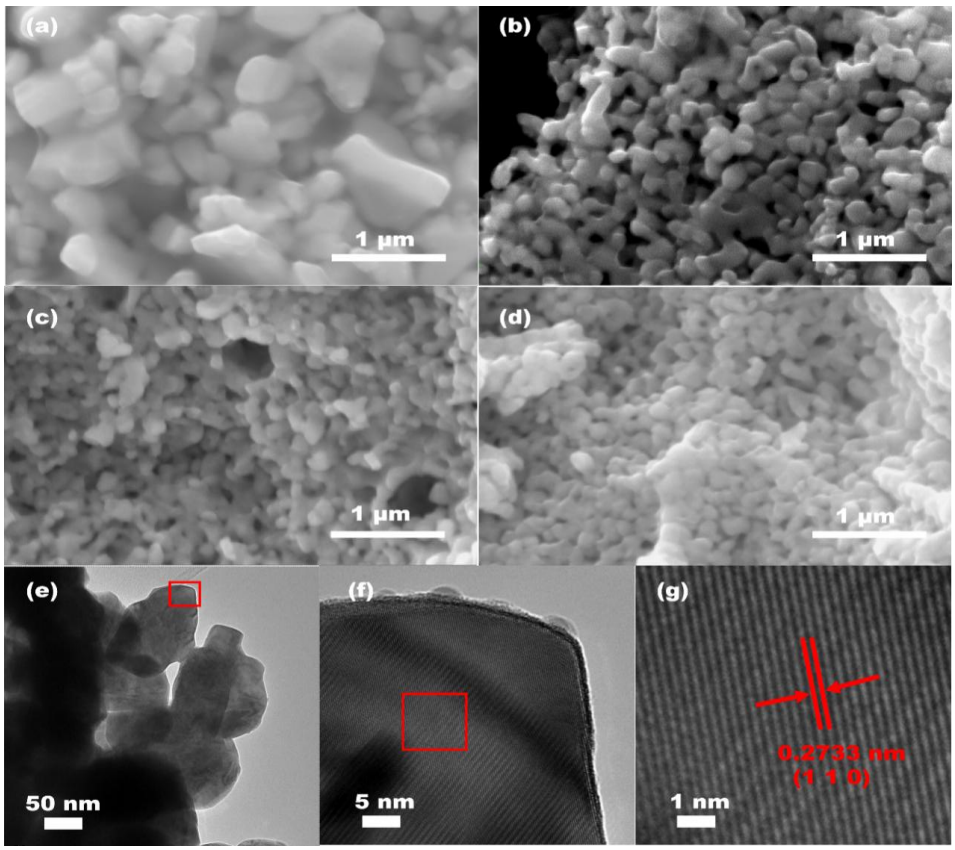

Figure 4. SEM images of $Bi_{1-x}Y_xFeO_3$ powder sample (a) $BiFeO_3$, (b) $Bi_{0.95}Y_{0.05}FeO_3$, (c)

$Bi_{0.90}Y_{0.10}FeO_3$, and (d) $Bi_{0.85}Y_{0.15}FeO_3$. (e)TEM images, (f) HRTEM images of nano $Bi_{0.90}Y_{0.10}FeO_3$ particles, and (g) high magnification image of the region marked with a red box in (f).

3.4. Magnetic Properties

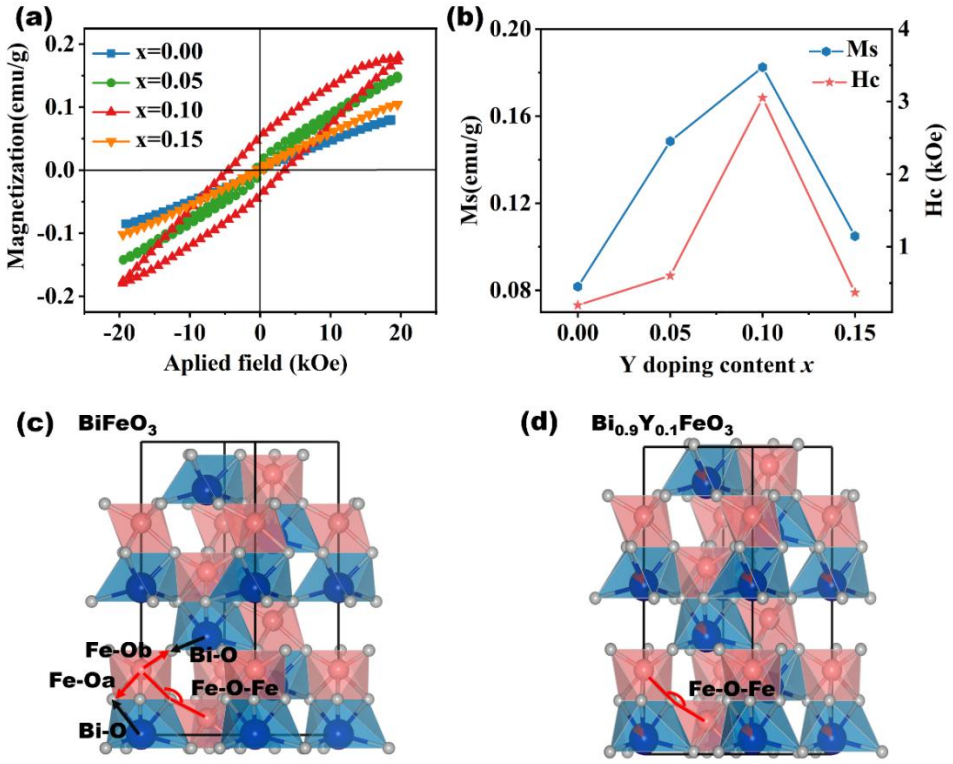

Figure 5. (a) M–H curves of $Bi_{1-x}Y_xFeO_3$. (b) Variation curve of Ms and Hc with Y doping content. Schematic diagram of the crystal structure (c) $BiFeO_3$ and (d) $Bi_{0.90}Y_{0.10}FeO_3$.

The magnetic properties of $Bi_{1-x}Y_xFeO_3$ were investigated by the room temperature magnetic hysteresis (M–H) curve and showed in **Fig.5** (a) and (b). The M–H curve of $BiFeO_3$ exhibits a linear pattern with the increase of the magnetic field, indicating the antiferromagnetic nature [22, 33]. After doping Y^{3+}, the M–H curves show a small open loop, suggesting a weak ferromagnetic behavior. In overall, Y^{3+} substitution can effectively enhance the magnetism of $BiFeO_3$. The magnetic saturation (Ms) of the samples first increases and then decrease with the increase of Y doping content, reaching the maximum value when x = 0.10. Owing to the non-magnetic nature of the Y element, it has no direct contribution to ferromagnetic enhancement. FeO6 octahedron distortion caused by Y doping is the main reason for ferromagnetic enhancement. Three-dimensional (3D) unit cell models of $BiFeO_3$ and $Bi_{0.90}Fe_{0.10}O_3$ are constructed using crystal refinement data to obtain specific bond and Angle information, as shown in Fig. 5(c) and (d). After doping Y, the Bi–O bond length is reduced from 2.2867 Å (x = 0.00) to 2.2596 Å (x = 0.10). The length of the Fe–O_a bond increases from 1.9438 Å (x = 0.00) to 2.0070 Å (x = 0.10), and the Fe−O_b bond decreases from 2.1125 Å (x = 0.00) to 2.0128 Å (x = 0.10). The change in the length of Fe–O_a and Fe–O_b bonds directly causes the Fe−O−Fe bond angle to increase from 155.6444° (x = 0.00) to 158.5398° (x = 0.10). The variation of the Fe−O−Fe bond angle will lead to the tilt of FeO6 octahedron, thus releasing the potential magnetic moments [34, 35]. With the continuous increase Y content to 0.15, the Ms decreases. A similar phenomenon is observed in Mn-doped $BiFeO_3$ prepared by Tian et al [35]. They believed that the change of crystal structure symmetry was the main reason. In this work, XRD spectrum show that the crystal structure transforms from rhombohedral to orthogonal (x = 0.15) with higher symmetry. The improved symmetry will alleviate the distortion of FeO6 octahedron and restore the modulated spiral spin structure. The coercive

force (Hc) displays a similar trend to Ms. The Y-doped $BiFeO_3$ decrease the grain size and distort the lattice which has influence on surface anisotropy and crystal stress, thus changing the Hc value.

3.5. EMA Performance

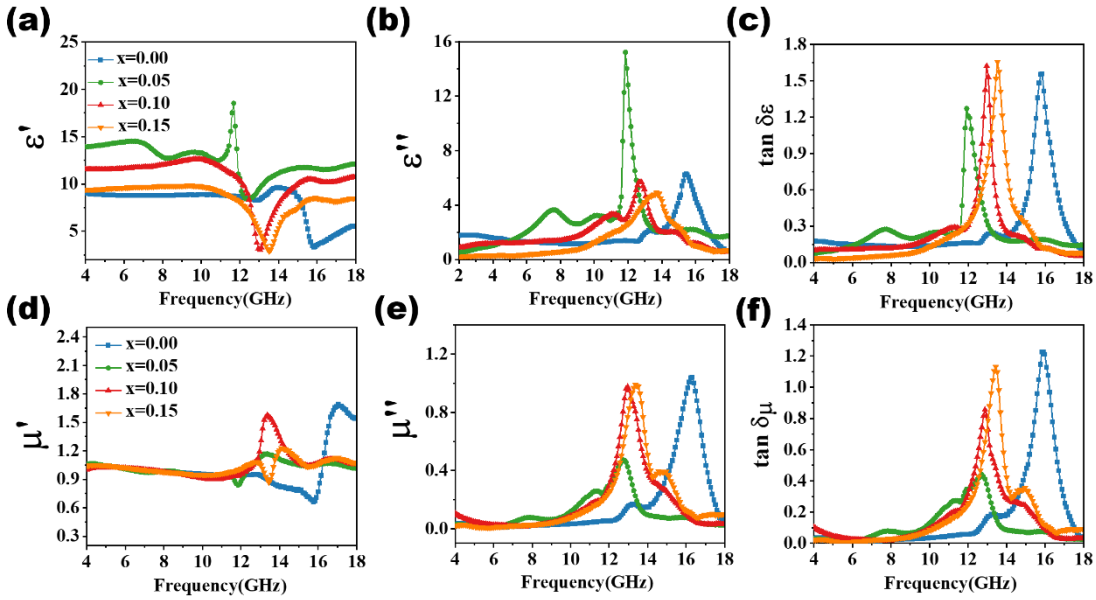

Figure 6. EM parameters of $Bi_{1-x}Y_xFeO_3$ (a) ε', (b) ε'', (c) dielectric loss tangent, (d)μ', (e) μ'', and (f) magnetic loss tangent.

The EMA performance is determined by electromagnetic (EM) parameters (ε', ε'', μ', and μ''). ε' and μ' represent the storage capacity of EMW energy, while ε'' and μ'' represent the attenuation capacity of EMW energy [36, 37]. The ε' and ε'' of $Bi_{1-x}Y_xFeO_3$ are shown in **Fig. 6**(a) and (b). The permittivity of $Bi_{0.95}Y_{0.05}FeO_3$ and $Bi_{0.90}Y_{0.10}FeO_3$ is higher than that of pure $BiFeO_3$, indicating the stronger the EMW energy storage and attenuation ability. The EMA properties are dependent on dielectric loss and magnetic loss ability. For dielectric loss, it can be evaluated by dielectric loss tangents ($\tan\delta\varepsilon = \varepsilon''/\varepsilon'$). From Fig. 6(c), several resonance peaks appear on the $\tan\delta\varepsilon$ curve, indicating the existence of multi-polarization. Dipolar polarization and interfacial polarization are major contributions to dielectric loss in the 2–18 GHz range [38, 39]. The shift off-center of Fe^{3+} in FeO6 octahedron, generating electric dipoles, which is the origin of dipolar polarization in $BiFeO_3$ [8]. The hysteresis and rotation of the electric dipole in the electric field create relaxation and help to dissipate EMW energy [40, 41]. Owing to the increase of Fe^{3+} concentration (Fig. 2(d)), the dielectric loss of Y-doped $BiFeO_3$ increase with the increase of Y doping content. In addition, Y^{3+} with smaller ions radius replaces Bi^{3+}, which intensifies the FeO6 distortion and leads to a stronger polarization effect. Moreover, abundant oxygen vacancy exists in $Bi_{1-x}Y_xFeO_3$ samples, which can act as dipole core to generate orientated polarization, effectively converting EMW energy into other energy forms [42]. In $Bi_{1-x}Y_xFeO_3$, the adjacent grains separate by highly resistive grain boundaries, forming rich hetero interfaces. Under the external electric field, the charges rearrange and accumulate at the grain boundaries, which build up interfacial polarization. In addition, interfacial polarization generated between the powder samples and paraffin is inevitable, which also helps to dissipate EM energy [43]. Cole-Cole semicircles are usually used to verify the relaxation process of EMA materials based on the Debye relaxation theory [44]. It can be described by the following equation:

$$\left(\varepsilon' - \frac{\varepsilon_s+\varepsilon_\infty}{2}\right)^2+\left(\varepsilon''\right)^2=\left(\frac{\varepsilon_s-\varepsilon_\infty}{2}\right)^2 \quad (1)$$

where ε_s is the static permittivity and ε_∞ represent the permittivity at the high frequency limit. **Fig. 7**(a) shows the Cole-Cole diagram of

$Bi_{0.90}Y_{0.10}FeO_3$. Two Cole–Cole semicircles are observed, implying the existence of two Debye relaxation polarization. The oxygen vacancies and non-centrosymmetrical Fe–O bond, which provide conditions for dipolar polarization. The hetero-interface form in the adjacent grain, resulting in strong interfacial polarization. Notably, the resonance peak gradually shifts to the low frequency region with increased the doping contents of Y, showing that Y doping can regulate the attenuation ability of $BiFeO_3$ to EMW in different frequency.

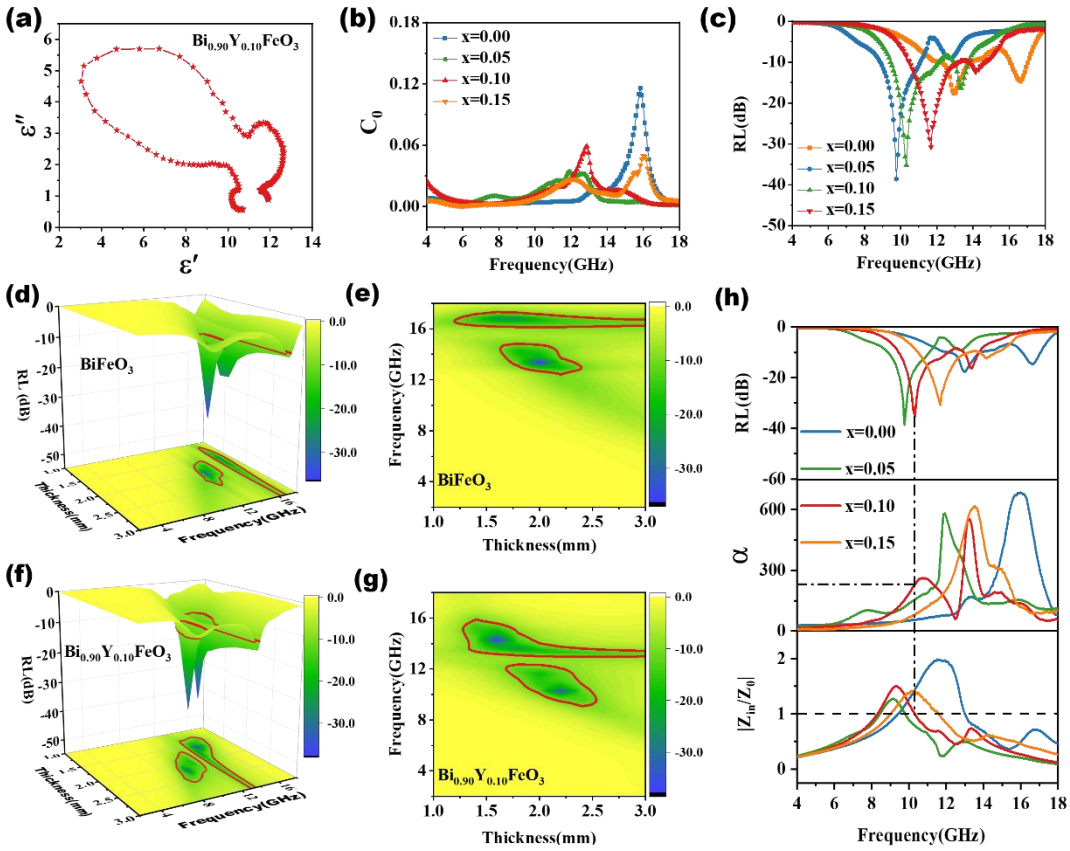

Figure 7. (a) Cole-Cole circle of $Bi_{0.90}Y_{0.10}FeO_3$. (b) C_0 of all the samples. (c) RL of $Bi_{1-x}Y_xFeO_3$ samples at simulated thickness 2.2 mm. 3D and 2D contour of the RL with frequency and thickness of (d and e) $BiFeO_3$ and (f and g) $Bi_{0.90}Y_{0.10}FeO_3$. (h) RL of $Bi_{1-x}Y_xFeO_3$ samples and corresponding attenuation constant (α) and impedance matching ($|Z_{in}/Z_0|$) at 2.2mm.

Table 2. Ferrite-based EMW absorbers.

EMW absorber	RL		EAB		Ref.
	RL_{min}(dB)	d(mm)	EAB(GHz)	d(mm)	
$Y_{1-x}Sr_xFeO_3$	–30.87	2.2	2.4	2.2	[7]
$BiFe_{0.95}Mn_{0.05}O_3$	–29.41	2.2	2.7	2.2	[35]
$La_{0.9}Ba_{0.1}FeO_3$	–30.04	3.2	2.1	3.2	[2]
$Bi_{0.9}Sm_{0.1}FeO_3$	–32.9	2.0	3.1	2.2	[16]
$Bi_{0.9}Nd_{0.1}FeO_3$	–33.7	2.0	2.8	2.0	[45]
CNT/$Ni_{0.5}Zn_{0.5}Fe_2O_4$	–19.34	3.0	1.2	3.0	[46]
$BiFeO_3$/epoxy resin	–40.5	3.0	1.3	3.0	[11]
$BiFeO_3$/RGO	–28.68	1.55	2.1	1.6	[47]
$Bi_{0.9}Y_{0.1}FeO_3$	–35.19	2.2	3.3	2.2	**This work**

Permeability is another important parameter to access EMA properties. As shown in Fig. 6(d) and (e), the μ' of all the samples show a similar flat trend with the same values in the range of 4–11 GHz and a huge fluctuation in 11–18 GHz. This phenomenon suggests that Y doping can changes the EMW energy storage capacity of $BiFeO_3$ at high frequencies, but has little effect on low frequencies. The μ'' value of Y-doped $BiFeO_3$ samples is larger than that of pure $BiFeO_3$ in the frequency range of 2–14 GHz. This may be attributed to the enhancement of Ms [45]. Magnetic tangent loss ($\tan\delta\mu = \mu''/\mu'$) is applied to study the magnetic loss ability of $Bi_{1-x}Y_xFeO_3$, as shown in Fig. 6(f). For magnetic absorber, magnetic loss mainly comes from ferromagnetic resonance effect and eddy current loss [14]. The strong resonance peaks found in the high frequency region can be ascribed to exchange resonance, which usually occur in nanoparticles [43]. The resonance peaks of $Bi_{1-x}Y_xFeO_3$ move to low frequency with the increase of Y content. C_0 ($C_0 = \mu''(\mu')^{-2}f^{-1}$) is used to elevate the impacts of eddy current loss on magnetic loss [39]. As shown in Fig. 7(b), the C_0 valves of all samples are almost constant in the range of 4–10 GHz, indicating that eddy current effect is dominant in this frequency region. The fluctuations observed in the 10-18 GHz range are ascribed to resonance effects [48]. The similar value of $\tan\delta\mu$ and $\tan\delta\varepsilon$ indicate that both dielectric and magnetic characteristics contribute to the attenuation of EMW in $Bi_{1-x}Y_xFeO_3$.

The EMA performance is assessed by RL curves according the transmission line theory, which is calculated as the following equation [49, 50]:

$$RL(dB) = 20\lg\left|\frac{Z_{in}-Z_0}{Z_{in}+Z_0}\right| \quad (2)$$

$$Z_{in} = Z_0\sqrt{\frac{\mu_r}{\varepsilon_r}}\tanh\left(j\frac{2\pi fd}{c}\sqrt{\mu_r\varepsilon_r}\right) \quad (3)$$

where Z_{in} and Z_0 is impedance of absorber and air, respectively. ε_r is complex permittivity ($\varepsilon_r = \varepsilon' - j\varepsilon''$) and μ_r is complex permeability ($\mu_r = \mu' - j\mu''$). f, c, and d represent the frequency, the speed of light and the matching thickness. The RL value is less than −10 dB, representing that 90% of the EMW can be absorbed, and the corresponding frequency region is referred to EAB. Fig. 7(c) shows the RL value of $Bi_{1-x}Y_xFeO_3$ samples at the matching thickness of 2.2 mm. The minimum RL value of pure $BiFeO_3$ is –17.69 dB and the EAB is 2.59 GHz. After doping Y^{3+}, stronger absorption intensity and broader EAB can be achieved. For Y doping $BiFeO_3$ samples, the minimum RL values are –38.61 dB (x = 0.05) at 9.76 GHz, –35.19 dB (x = 0.10) at 10.32 GHz, and –30.78 dB (x = 0.15) at 11.68 GHz, respectively. The corresponding EAB are 2.17 GHz (x = 0.05), 3.29 GHz (x = 0.10), and 3.08 GHz (x = 0.15), respectively. After doping Y, the peaks of minimum RL shift to lower frequency region, which is consistent with the movement of the resonance peaks of $\tan\delta\varepsilon$ and $\tan\delta\mu$. The optimal EMA performance can be obtained when the Y doping content is 0.10. Fig. 7(d–g) show the 3D RL diagram of $BiFeO_3$ and $Bi_{0.90}Y_{0.10}FeO_3$ at different matching thickness. Obviously, Y doping can regulate the EMA performance of $BiFeO_3$. Comparison with the ferrite-based absorber in Table 2, $Bi_{0.90}Y_{0.10}FeO_3$ display much better EMA performance with stronger absorption intensity and wider EAB, indicating highly potential for application in EMA.

Impedance matching ($|Z_{in}/Z_0|$) is a prerequisite for obtaining excellent absorption performance. The $|Z_{in}/Z_0|$ value equal to 1 represent the optimal impedance matching characteristic, that is, the EMW enter the absorber freely. Subsequently, the incident EMW is converted into other energy forms through series of loss mechanisms. The EMW loss capability can be evaluated by attenuation constant (α), which is expressed by the equation:

$$\alpha = \frac{\sqrt{2}\pi f}{c}\sqrt{(\mu''\varepsilon'' - \mu'\varepsilon') + \sqrt{(\mu''\varepsilon'' - \mu'\varepsilon')^2 + (\mu'\varepsilon'' + \mu''\varepsilon')^2}} \quad (4)$$

The higher the α value, the stronger the attenuation ability of EMW energy. From Fig. 7(f), the minimum RL value of all the samples is obtained when the $|Z_{in}/Z_0|$ value is 1, but the α value is not the maximum. This result show that impedance matching is the determinant of obtaining strong EMW absorption ability. Moreover, simple $BiFeO_3$ show much poor impedance matching property than the Y doping

$BiFeO_3$ samples. The Y doping effectively adjusts the permittivity and permeability of $BiFeO_3$, and achieves the balance of EM parameters, thus optimizing the impedance matching properties. The Y-doped $BiFeO_3$ exhibit much better attenuation ability than that of simple $BiFeO_3$ in the frequency range of 4–14 GHz, which confirms that Y-doped $BiFeO_3$ has better EMA performance at this frequency range.

Based on the above analysis, the possible EMW loss mechanism of Y-doped $BiFeO_3$ can be concluded as follow: firstly, oxygen vacancy and non-centrosymmetrical of Fe–O bond leads to dipolar polarization under external electric field. Then, the reduction of grain size is conducive to the formation of more heterogeneous interfaces, resulting in stronger interface polarization. Finally, accompanied by resonance and eddy current loss effects, the EM energy is effectively converted into other forms of energy.

4. Conclusions

In this paper, $Bi_{1-x}Y_xFeO_3$ was synthesized by sol-gel method. XRD structure refinement show that the crystal structure of $Bi_{1-x}Y_xFeO_3$ transferred from rhombic perovskite structure ($x \leq 0.10$) to orthorhombic structure ($x = 0.15$). The grain size decrease with the increase of the Y doping content due to the reduced the concentration of oxygen vacancy. The Y doped $BiFeO_3$ show great improvements in saturation magnetization than pure $BiFeO_3$ due to the distortion of FeO6 octahedron. Interfacial polarization, dipolar polarization, eddy current loss and ferromagnetic resonance effect are contributed to the improvement of the EMA performance. The minimum RL of –35.19 dB and the EAB of 3.29 GHz can be achieved at the Y doping amount of 0.10.

Acknowledgements

This work is financially supported by the National Natural Science Foundation of China (Grant No. 52261004), Guangxi Natural Science Foundation of China (Grant No. 2021GXNSFDA075009).

Declaration of Competing Interest

The authors declare that they have no known competing financial interests or personal relationships that could have appeared to influence the work reported in this paper.

References

1. Y. Liu, Y. Lin, H. Yang, Facile fabrication for core-shell $BaFe_{12}O_{19}$@C composites with exc ellent microwave absorption properties, J. Allo ys Compd. 805 (2019) 130-137.
2. L. Huang, L. Cheng, S. Pan, Q. Yao, Q. Long, M. Wang, Y. Chen, H. Zhou, Influence of A-sit e doping barium on structure, magnetic and mi crowave absorption properties of $LaFeO_3$ cera mics powders, J Rare Earths 40(7) (2022) 110 6-1117.
3. S. Aman, N. Ahmad, M.H. Alhossainy, H. Alb alawi, M. Morsi, T.I. Al-Muhimeed, A.A. AlO baid, Structural, magnetic, electrical and micro wave properties of spinel ferrites, J Rare Earth s 40(3) (2022) 443-450.
4. J. Ouyang, Z. He, Y. Zhang, H. Yang, Q. Zhao, Trimetallic FeCoNi@C nanocomposite hollow spheres derived from metal-organic framewor ks with superior electromagnetic wave absorpt ion ability, ACS Appl. Mater. Interfaces 11(42) (2019) 39304-39314.
5. F. Wu, M. Ling, L. Wan, P. Liu, Y. Wang, Q. Z hang, B. Zhang, Three-dimensional FeMZn (M = Co or Ni) MOFs: Ions coordinated self-a ssembling processes and boosting microwave absorption, Chem. Eng. J. 435 (2022) 130020.
6. F. Gan, Q. Rao, J. Deng, L. Cheng, Y. Zhong, Z. Lu, F. Wang, J. Wang, H. Zhou, G. Rao, Co ntrollable architecture of ZnO/FeNi composite s derived from trimetallic ZnFeNi layered dou ble hydroxides for high-performance electrom agnetic wave absorbers, Small (2023)230025 7 .
7. M. Wang, L. Cheng, L. Huang, S. Pan, Q. Yao, C. Hu, Q. Liang, H. Zhou, Effect of Sr doped t he $YFeO_3$ rare earth ortho-ferrite on structure, magnetic properties, and microwave absorptio n performance, Ceram. Int. 47(24) (2021) 341 59-34169.
8. L. Huang, L. Cheng, S. Pan, Y. He, C. Tian, J. Yu, H. Zhou, Effects of Sr doping on the struct ure, magnetic properties and microwave absor ption properties of $LaFeO_3$ nanoparticles, Cera m. Int. 46(17) (2020) 27352-27361.
9. F. Hu, H. Nan, M. Wang, Y. Lin, H. Yang, Y. Q iu, B. Wen, Construction of core-shell $BaFe_{12}O_{19}$@MnO_2 composite for effectively enhanci ng microwave absorption performance, Cera m. Int. 47(12) (2021) 16579-16587.
10. W. Azeem, S. Riaz, A. Bukhtiar, S. Sajjad Hus sain, Y. Xu, S. Naseem, Ferromagnetic orderin

g and electromagnons in microwave synthesized $BiFeO_3$ thin films, J. Magn. Magn. Mater. 475 (2019) 60-69.
11. S.N.A. Rusly, I. Ismail, K.A. Matori, Z. Abbas, A.H. Shaari, Z. Awang, I.R. Ibrahim, F.M. Idris, M.H. Mohd Zaid, M.K.A. Mahmood, I. H. Hasan, Influence of different BFO filler content on microwave absorption performances in $BiFeO_3$/epoxy resin composites, Ceram. Int. 46(1) (2020) 737-746.
12. S. Farhadi, N. Rashidi, Microwave-induced solid-state decomposition of the $Bi[Fe(CN)_6]\cdot 5H_2O$ precursor: A novel route for the rapid and facile synthesis of pure and single-phase $BiFeO_3$ nanopowder, J. Alloys Compd. 503(2) (2010) 439-444.
13. L. Wang, Z. Du, L. Xiang, D. Hou, S. Zhu, J. Zhu, Y. Mai, R. Che, The ordered mesoporous carbon coated graphene as a high-performance broadband microwave absorbent, Carbon 179 (2021) 435-444.
14. P.-A. Yang, Y. Huang, R. Li, X. Huang, H. Ruan, M. Shou, W. Li, Y. Zhang, N. Li, L. Dong, Optimization of Fe@Ag core–shell nanowires with improved impedance matching and microwave absorption properties, Chem. Eng. J. 430 (2022).
15. G. Chen, L. Zhang, B. Luo, H. Wu, Optimal control of the compositions, interfaces, and defects of hollow sulfide for electromagnetic wave absorption, J. Colloid Interface Sci. 607 (2022) 24-33.
16. C. Tian , Q. Yao , Z. Tong , H. Zhou, G. Rao, J. Deng , Z. Wang , J. Wang, Effects of Sm-doping on microstructure, magnetic and microwave absorption properties of $BiFeO_3$, J rare earth.39 (2021) 835-843.
17. M.T. Kebede, S. Devi, V. Dillu, S. Chauhan, Influence of novel Cd–Ni co-substitution on structural, magnetic, optical and photocatalytic properties of $BiFeO_3$ nanoparticles, J. Alloys Compd. 894 (2022) 162552.
18. X. Gao, Y. Wang, Q. Wang, X. Wua, W. Zhang, M. Zong, L. Zhang, Facile synthesis of a novel flower-like $BiFeO_3$ microspheres/graphene with superior electromagnetic wave absorption performances, Ceram. Int 45 (2019) 3325-3332.
19. X. Wang, Z. Wu, B. Li, W. Chen, J. Zhang, J. Mao, Inclusions modification by rare earth in steel and the resulting properties: A review, J Rare Earth (2024) 431-445.
20. L. Hou, L. Xia, R. Zhou, J. Li, R. Li, Z. Zhao, G. Yuan, A. Duan, Effect of yttrium on catalytic performance of Y-doped TiO_2 catalysts for propane dehydrogenation, J Rare Earth (2023) 962-971.
21. G.S. dos Reis, D. Pinto, S.F. Lütke, É. Lima, L.F.O. Silva, I.A.S. De Brum, G.L. Dotto, Adsorption of yttrium (Y^{3+}) and concentration of rare earth elements from phosphogypsum using chitin and chitin aerogel, J Rare Earth (2023) 775-782.
22. J. Guo, Z. Tong, Q. Liang, F. Gan, L. Wei, Q. Yao, J. Deng, Z. Lu, H. Zhou, Investigating the effect of Pr doping $BiFeO_3$ on the microwave absorption and magnetic properties, J. Magn. Magn. Mater. 549 (2022) 168957.
23. T.K. Lin, H.W. Chang, C.R. Wang, D.H. Wei, C.S. Tu, P.Y. Chen, Structure transition and enhanced multiferroic properties of Dy-doped $BiFeO_3$ thin films, Surface & Coatings Technology 435 (2022) 853-870.
24. Y. Li, H. Yang, W. Yang, Z. Hou, J. Li, H. Jin, J. Yuan, M. Cao, Structure, ferromagnetism and microwave absorption properties of La substituted $BiFeO_3$ nanoparticles, Mater. Lett. 111 (2013) 130-133.
25. P. Chen, J. Chen, Microwave-sintering enhanced photovoltaic conversion in polycrystalline Nd-doped $BiFeO_3$, Ceram. Int. 46(13) (2020) 20963-20973.
26. T.K. Lin, H.W. Chang, C.R. Wang, D.H. Wei, C.S. Tu, Multiferroic and nanomechanical properties of $Bi_{1-x}R_xFeO_3$ polycrystalline films (R = La, Pr, Sm, and Ho; x = 0–0.15), J. Alloys Compd. 846 (2020) 156080.
27. C. Li, Z. Zhang, J. Sui, X. Jiang, G.I.N. Waterhouse, Z. Zhang, L. Yu, Microwave-based synthesis of $(NiCo)_x/(MnO)_y$/C composites and their tunable wave absorption properties in the K band, Ceram. Int. 46(7) (2020) 9353-9362.
28. J. Wang, Z. Jia, X. Liu, J. Dou, B. Xu, B. Wang, G. Wu, Construction of 1D heterostructure NiCo@C/ZnO nanorod with enhanced microwave absorption, Nano-Micro Lett. 13(1) (2021) 175.
29. S. Liu, H. Luo, S. Yan, L. Yao, J. He, Y. Li, L. He, S. Huang, L. Deng, Effect of Nd-doping on structure and microwave electromagnetic properties of $BiFeO_3$, J. Magn. Magn. Mater. 426 (2017) 267-272.
30. F. Gan, Q. Yao, J. Deng, F. Wang, L. Cheng, Y. Chen, H. Zhou, Y. Zhong, H. Yang, Y. Zhao, L

ayered double hydroxides derived 3D flower-like FeNi@C microspheres as lightweight and high-efficient electromagnetic wave absorber, Carbon 196 (2022) 639-648.
31. X. Shi, Z. Liu, X. Li, W. You, Z. Shao, R. Che, Enhanced dielectric polarization from disorder-engineered Fe_3O_4@black TiO_{2-x} heterostructure for broadband microwave absorption, Chem. Eng. J. 419 (2021) 130020.
32. F.L. Wang, Y. Li, N. Wang, L. Zhu, A. Jain, Y. G. Wang, F.G. Chen, Enhanced magnetic, ferroelectric and optical properties of Sr and Co co-doped $BiFeO_3$ powders, J. Alloys Compd. 810 (2019) 151941.
33. Z. Hou, H. Zhou, L. Kong, H. Jin, X. Qi, M. Cao, Enhanced ferromagnetism and microwave absorption properties of $BiFeO_3$ nanocrystals with Ho substitution, Mater. Lett. 84 (2012) 110-113.
34. M. Kao, H. Chen, S. Young, J. Chiang, P. Chen, Structural transition and multiferroic properties of Pr- and Mn-doped $BiFeO_3$ Thin Films, J. Comput. Theor. Nanosci. 12(5) (2015) 786-791.
35. C. Tian, Z. Tong, L. Huang, Q. Yao, J. Deng, Q. Long, L. Cheng, Z. Wang, J. Wang, H. Zhou, G. Rao, Mn doping of $BiFeO_3$ for microstructure and electromagnetic characteristics, J Supercond Nov Magn 34(4) (2021) 1199-1207.
36. H. Wu, Z. Zhao, G. Wu, Facile synthesis of FeCo layered double oxide/raspberry-like carbon microspheres with hierarchical structure for electromagnetic wave absorption, J Colloid Interface Sci 566 (2020) 21-32.
37. X. Liang, Z. Man, B. Quan, J. Zheng, W. Gu, Z. Zhang, G. Ji, Environment-stable Co_xNi_y encapsulation in stacked porous carbon nanosheets for enhanced microwave absorption, Nano-Micro Lett. 12(1) (2020) 102.
38. Y. Yang, D. Xu, L. Kong, J. Qiao, B. Li, X. Ding, J. Liu, W. Liu, F. Wang, Construction of Ni-Zn bimetal sulfides heterostructured-hybrids for high-performance electromagnetic wave absorption, J. Colloid Interface Sci. 606 (2022) 1410-1420.
39. B. Zhao, Y. Li, Q. Zeng, B. Fan, L. Wang, R. Zhang, R. Che, Growth of magnetic metals on carbon microspheres with synergetic dissipation abilities to broaden microwave absorption, J. Mater. Sci. Technol. 107 (2022) 100–110.
40. X. Ding, L. Lyu, F. Wang, Y. Yang, J. Qiao, D. Xu, X. Zhang, L. Kong, J. Liu, Novel ternary Co_3O_4/CeO_2/CNTs composites for high-performance broadband electromagnetic wave absorption, J. Alloys Compd. 864 (2021) 158141.
41. X. Li, G. Tan, Multiferroic and magnetoelectronic polarizations in $BaFe_{12}O_{19}$ system, J. Alloys Compd. 858 (2021).
42. M. Qin, L. Zhang, X. Zhao, H. Wu, Lightweight Ni foam-based ultra-broadband electromagnetic wave absorber, Adv. Funct. Mater. 31(30) (2021) 2103436.
43. F. Gan, Q. Yao, L. Cheng, L. Zhang, Q. Liang, J. Guo, M. Wang, H. Zhou, Y. Zhong, Fabrication of $BaFe_{12}O_{19}/CeO_2$ composite for highly efficient microwave absorption, J. Alloys Compd. 897 (2022) 162964.
44. J. Cheng, L. Cai, Y. Shi, F. Pan, Y. Dong, X. Zhu, H. Jiang, X. Zhang, Z. Xiang, W. Lu, Polarization loss-enhanced honeycomb-like MoS_2 nanoflowers/undaria pinnatifida-derived porous carbon composites with high-efficient electromagnetic wave absorption, Chem. Eng. J. 431 (2022).
45. C. Tian, Q. Yao, Z. Tong, G. Rao, J. Deng, Z. Wang, J. Wang, H. Zhou, J. Zhao, The influence of Nd substitution on microstructural, magnetic, and microwave absorption properties of $BiFeO_3$ nanopowders, J. Alloys Compd. 859 (2021).
46. M.S. Mustaffa, R.S. Azis, N.H. Abdullah, I. Ismail, I.R. Ibrahim, An investigation of microstructural, magnetic and microwave absorption properties of multi-walled carbon nanotubes/$Ni_{0.5}Zn_{0.5}Fe_2O_4$, Sci Rep 9(1) (2019) 15523.
47. D. Moitra, S. Dhole, B.K. Ghosh, M. Chandel, R.K. Jani, M.K. Patra, S.R. Vadera, N.N. Ghosh, Synthesis and microwave absorption properties of $BiFeO_3$ nanowire-RGO nanocomposite and first-principles calculations for insight of electromagnetic properties and electronic structures, J. Phys. Chem. C 121(39) (2017) 21290-21304.
48. X. Shi, W. You, X. Li, L. Wang, Z. Shao, R. Che, In-situ regrowth constructed magnetic coupling 1D/2D Fe assembly as broadband and high-efficient microwave absorber, Chem. Eng. J. 415 (2021) 128951.
49. Y. Qiu, H. Yang, Y. Cheng, B. Wen, Y. Lin, Structure design of prussian blue analogue derived CoFe@C composite with tunable microwave absorption performance, Appl. Surf. Sci. 571 (2022).
50. X. Li, Z. Wu, W. You, L. Yang, R. Che, Self-as

sembly MXene-rGO/CoNi film with massive continuous heterointerfaces and enhanced magnetic coupling for superior microwave absorber, Nano-Micro Lett. 14(1) (2022) 73.